Journal of Catalysis 407 (2022) 342–352

Contents lists available at ScienceDirect

Journal of Catalysis

journal homepage: www.elsevier.com/locate/jcat

Nanometer-thick defective graphene films decorated with oriented ruthenium nanoparticles. Higher activity of 101 vs 002 plane for silane-alcohol coupling and hydrogen transfer reduction

Aicha Anouar [a,b], Rubén Ramírez Grau [a], Nadia Katir [b], Antonio Franconetti [c], Abdelkrim El Kadib [b,*], Ana Primo [a,*], Hermenegildo García [a,*]

[a] Instituto de Tecnología Química, Universitat Politècnica de València-Consejo Superior de Investigaciones Científicas, Av. De los Naranjos s/n, 46022 Valencia, Spain
[b] Euromed Research Center, Engineering Division, Euro-Med University of Fès (UEMF), Route de Meknes, Rond-point de Bensouda, 30070 Fès, Morocco
[c] Departamento Química Orgánica, Facultad de Química, Universidad de Sevilla, Profesor García Gonzalez 1, 41012 Sevilla, Spain

ARTICLE INFO

Article history:
Received 11 November 2021
Revised 16 January 2022
Accepted 7 February 2022
Available online 14 February 2022

Keywords:
Oriented ruthenium nanoparticles
Ruthenium nanoparticles supported on defective graphene
101 facet of ruthenium nanoparticles
Dehydrogenative silane-alcohol coupling
Catalytic hydrogen transfer reaction

ABSTRACT

Pyrolysis of ammonium alginate films containing $Ru(NH_3)_6Cl_3$ leads to the formation of Ru nanoparticles (NPs) supported on defective graphene films. The procedure allows controlling the preferential facet orientation of small Ru NPs (5–20 nm), either 002 when the pyrolysis is carried out under Ar atmosphere or the 002 and 101 planes for pyrolysis in the presence of H_2. Ru is a metal difficult to prepare in preferential facet orientation compared to noble metals due to its higher reactivity and smaller particle size. Theoretical calculations substantiated the inhibition of Ru(002) growth by H_2 adsorption, with restructuration to Ru(002–101) NPs. The defective graphene films of about 15 nm thickness containing one of the two types of Ru NPs (150 ng/cm^2) exhibit distinctive catalytic activity for the dehydrogenative coupling of silanes and alcohols and hydrogen transfer reduction of cyclohexanone. Comparison of turnover frequencies indicates that the 101 facet is more efficient than the 002 plane. Overall, this study illustrates that pyrolysis conditions can control the preferential crystallographic orientation of the growing Ru NPs and the relative catalytic activity of their specific crystallographic planes.

1. Introduction

Transition metal nanoparticles (NPs) supported on large area solids are general heterogeneous catalysts,[1] being able to promote a wide range of reaction types, including oxidations [2,3], reductions [4], homo- and crosscouplings [1,2,5], rearrangements [6] and acid-base reactions [7,8]. A continuous interest in this area is to develop strategies to optimize their catalytic activity [9,10]. This goal has been achieved, among other ways, by decreasing the particle size [11], selection of suitable supports exhibiting adequate metal-support interactions [12] and by controlling the crystal phase and particle morphology [4].

Metal nanoparticles display different physical and chemical properties compared to bulk metals, making them very attractive in catalysis [13]. The intrinsic properties of a metal nanoparticle arise mainly from its size, shape and crystallinity. Besides the effect of size, the preferential crystallographic orientation of nanoparticles may drastically improve their catalytic activity [14]. Anisotropic nanoparticles are generally prepared through colloidal synthesis, involving the use in solution of stabilizing ligands, which strongly bind to certain facets limiting their growth and apparently favoring the crystal growth in different planes, resulting in selectively-oriented nanoparticles [15]. While bulky long chain surfactants are ubiquitously used for such purpose [16], small gas molecules including hydrogen and carbon monoxide have also been found to provide selectively-oriented nanoparticles [17,18]. Palladium and platinum nanocrystals with a defined crystallographic shape and facet have been synthesized using CO or H_2 as growth directing agents. In these reports, CO or H_2 molecules adsorb strongly on the exposed crystallographic facet during the formation of the nanocrystals and restrict their growth [19–22]. A control of the crystallographic facet exposed by the nanoparticle would have a significant influence on its activity and its selectivity in the catalysis of different reactions [17,18]. For instance, Pt can selectively catalyze different types of chemical reactions, with the {100} and {210} facets being more active for reactions involving H_2 and CO, respectively [23]. In another example, Ag (110) and Ag (100) facets have better activity for the electrocatalytic

* Corresponding authors at: Instituto de Tecnología Química, Universitat de Valencia, Spain.
E-mail address: hgarcia@qim.upv.es (H. García).

https://doi.org/10.1016/j.jcat.2022.02.007
0021-9517/

reduction of CO_2 to CO, a result attributed to the strong adsorption of carboxyl groups on the {1 1 0} and {1 0 0} faces [24].

Although the colloidal synthesis has given rise to extremely active catalysts [14], their physical state in suspension hinders their recovery from the reaction medium and makes their use in catalysis less convenient than supported metal nanoparticles. To tackle these drawbacks, oriented nanoparticles must be supported on a large surface area material such as graphene. The latter raised as a unique support in heterogeneous (photo)catalysis [25–28].

In this context, the simultaneous formation of metal NPs and defective graphenes by pyrolysis of natural polysaccharides adsorbing metal salts has been reported [29,30]. This procedure ensures a strong interaction between the metal NP and defective graphene, as deduced by the size and morphology of the metal NPs [31,32]. In addition to the strong grafting, these metal NPs on defective graphene can exhibit a preferential facet [30,32]. It was proposed that during the pyrolysis, the graphene sheet is templating the formation of the metal NP by epitaxial growth, thus resulting in the development of the crystallographic plane that better matches the hexagonal graphene arrangement [30]. Oriented metal NPs grafted on few layers defective graphene have shown an extremely high activity for this type of materials [33,34]. The concept has been proved for gold [33], copper [34], platinum [35], and silver characterized by particles with platelet morphology and large lateral size (50–90 nm) [29]. Considering that experimental studies and theoretical modeling indicate different catalytic activities for different planes of metal NPs [36–42], it is of interest to expand the study of the specific catalytic activity of different crystal planes to other metals, particularly those that are difficult to be obtained with preferential crystallographic orientation such as Ru [43]. Studies on the specific reactivity of Ru facets is up to now very limited in comparison to Pt, Au and other metals due to higher difficulty in the selective preparation of oriented Ru NPs [14,15]. The reluctance of Ru NPs to form oriented particles derives from the high reactivity of Ru and its tendency to form smaller NPs in comparison with noble metals. Therefore, it is of interest to expand the method of simultaneous defective graphene and metal synthesis to more challenging metals, such as Ru.

Herein, the preparation of nanometer-thick films of small Ru NPs (5–20 nm) exposing preferentially two different crystallographic planes grafted on few layers defective graphene exhibiting very high catalytic activity for dehydrogenative coupling of hydrosilanes and alcohols and hydrogen transfer reduction of cyclohexanone as two model reactions is reported. The preferential crystallographic orientation depends on the synthesis conditions. In this way, defective graphene films having Ru NPs with preferential 002 facet ($\overline{Ru}$(0 0 2)/G, $\overline{Ru}$ meaning oriented Ru NP) or preferential 002 and 101 facets ($\overline{Ru}$(002–101)/G) can be prepared depending on the absence or presence of hydrogen. It is noteworthy to mention that in our previous studies [33,34,44], when metal NPs were grown on G films they exhibited only one preferential orientation and that tailoring of the crystallographic orientation by interaction with gas molecules has not yet been reported. In addition, the particle size of the oriented metal NP is notably smaller in the case of Ru respect to the previously reported metals [29]. Comparison of the catalytic activity of these two samples provides experimental evidence of the specific catalytic reactivity for each of these two crystallographic planes. The performance of $\overline{Ru}$ NPs has been compared with those obtained for an analogous Ru/G in where Ru NPs of much smaller particle size, but lacking preferential crystallographic, are homogeneously dispersed on the same type of graphene. It was found that these small Ru NPs exhibit much lesser activity in spite of their much smaller diameter. Data will be presented showing that the intrinsic catalytic activity is dramatically enhanced when the Ru NPs are strongly interacting with the defective graphene film and that the 101 facet exhibits higher catalytic activity than the 002 plane. In addition, the catalytic activity of oriented Ru NPs also compares favorably with other benchmark catalysts reported in the literature for dehydrogenative silane-alcohol coupling and cyclohexanone reduction by alcohols. Since catalysis is constantly searching for more efficient catalysts, the present study shows how preferential facet orientation and grafting on graphene can serve to develop more advanced heterogeneous catalysts.

2. Experimental

2.1. Materials

All reagents used in this work were purchased from Sigma-Aldrich and were used as received without further purification.

2.2. Preparation of catalysts

2.2.1. Preparation of Ru/G

2 g of sodium alginate (Lot #MKBZ5563V) were dissolved in 50 ml of MilliQ water under magnetic stirring. The stirring was maintained for 12 h to ensure complete dissolution of sodium alginate. The resulting solution is dropped into a 2 M HCl solution. The alginic acid hydrogel in the form of microspheres was stirred in the acidic solution for 3 h, before copious washing with MilliQ water until washing waters became neutral. The microspheres are then immersed in an aqueous solution of $RuCl_3{\cdot}xH_2O$ (70.5 mg in 100 ml of MilliQ water) for 16 h. The hydrogels were dehydrated by gradual exchange of water by ethanol using consecutively four mixtures with a relative water–ethanol proportion of 75–25, 50–50, 25–75 and 0–100. Each water to ethanol exchange was carried out by magnetic stirring at 50 rpm for 2 h at room temperature. Then, the resulting alcogels were dried with an automated supercritical CO_2 dryer. The aerogels were pyrolyzed at 5 °C/min until reaching a temperature of 900 °C under Ar atmosphere for 1 h. A content of Ru of 1% was determined by ICP-OES by dispersing a certain amount of Ru/G in 8 ml of *aqua regia* and heating at 100 °C for 24 h.

2.2.2. Preparation of $\overline{\boldsymbol{Ru}}$(002)/G

Alginic acid from Sigma-Aldrich (Lot #SLBL2988V) was first dispersed in 9 ml of MilliQ water under magnetic stirring followed by the addition of 1 ml of aqueous NH_4OH solution (25%) to ensure its complete dissolution. After stirring for 2 h, the resulting solution of ammonium alginate was filtered through a syringe of 0.45 μm pore diameter to remove eventual impurities present in the powder. 148 mg of hexaaminеruthenium(III) chloride purchased from Sigma-Aldrich (Lot#MKCF0161) was dissolved in 200 μL of MilliQ water. 3 ml of filtered ammonium alginate solution was, then, added to the ruthenium complex solution and the mixture is left under stirring for 3 h. The resulting suspension was, then, filtered through a syringe of 0.45 μm diameter. The films were prepared by casting the solution on a freshly cleaned quartz plate (1×1 cm^2) at 4000 rpm for 30 s. The films were dried at 60 °C for 1 h prior to submit them to pyrolysis under Ar atmosphere at a heating rate of 5 °C/min up to 1000 °C and a dwelling time of 1 h at the final temperature. The plates were allowed to cool at room temperature under Ar atmosphere. The amount of Ru was determined by ICP-OES by immersing the plates into *aqua regia* for 24 h and analyzing the Ru content of the resulting solution. Although films with various Ru contents were prepared with identical facet orientation, most of the catalytic experiments reported here were performed with the films having 1.34×10^{-9} $mol_{Ru} \times cm^{-2}$.

*2.2.3. Preparation of **Ru**(002–101)/G*

Alginic acid purchased from Sigma-Aldrich (Lot #SLBL2988V) was first dispersed in 9 ml of MilliQ water followed by the addition of 1 ml of aqueous NH_4OH solution (25 %) to ensure its complete dissolution. After stirring for 2 h, the resulting solution of ammonium alginate was filtered through a syringe with a Nylon filter of 0.45 μm pore diameter to remove eventual impurities present in the powder. 148 mg of hexaammineruthenium (III) chloride purchased from Sigma-Aldrich (Lot#MKCF0161) was separately dissolved in 200 μL of MilliQ water. 3 ml of the filtered ammonium alginate solution was added to the metallic solution and the resulting mixture was left under stirring for 3 h. The color of the resulting suspension turned dark brown. The resulting suspension was then filtered through a syringe of 0.45 μm diameter. The films were prepared by casting the solution on a freshly cleaned quartz plate (1×1 cm^2) at 4000 rpm for 30 s. The films were dried for 1 h at 60 °C prior to pyrolysis under 5 % H_2/ 95% Ar atmosphere at a heating rate of 5 °C/min up to 1000 °C and dwelling time of 1 h at the final temperature. The amount of Ru was determined by ICP-OES analysis by immersing the plates into *aqua regia* for 24 h and analyzing the Ru content of the resulting solution. Films of different Ru loadings were prepared. However, most of the catalytic experiments were performed using films containing 1.76×10^{-9} $mol_{Ru} \times cm^{-2}$.

2.2.4. Catalysts characterization

XRD patterns were recorded using a Cubix Pro PANanalytical diffractometer. Raman spectra were recorded using a 514 nm excitation laser on a Renishaw Raman spectrometer equipped with a LEICA microscope. FESEM images were recorded using a ZEISS Ultra 55 microscope. HRTEM images were recorded in a JEOL JEM2100F under an accelerating voltage of 200 kV. AFM images were recorded using a Bruker multimode microscope under tapping mode. XP spectra were measured on a SPECS spectrometer using a monochromatic X-Ray source (Al and Mg) operating at 200 W.

2.2.5. General procedure for the dehydrogenative coupling of dimethylphenylsilane with alcohols

All reagents were purchased from Sigma-Aldrich and used as received without additional purification steps. To 1 mmol of dimethylphenylsilane, 1.5 ml of the alcohol is added followed by the addition of the catalyst (3 rigid plates of $\overline{Ru}$(002–101)/G or $\overline{Ru}$(002)/G films or 3 mg of Ru/G powder). The reaction was stirred at 250 rpm for 4 h or 24 h at room temperature. The catalyst was collected by filtration and the reaction products were analyzed using GC–MS using *n*-dodecane as internal standard. TOF values were calculated considering all Ru atoms in the sample. Calculation of TOF was made using the following equations:

TON: Amount of converted reactant (mol)/amount of Ru (mol)

TOF: TON/Time(h)

*2.2.6. Reusability of Ru/G, **Ru**(002–101)/G and **Ru**(002)/G*

Reusability of Ru/G as microspheres was carried out using 10 mmol of dimethylphenylsilane, 15 ml of butanol and 30 mg of Ru/G in a 130 ml reactor. Between each catalytic run, the beads are recovered and washed once with butanol and twice with ether, dried and used in the following run. Reusability of $\overline{Ru}$(002–101)/G and $\overline{Ru}$(002)/G quartz plates was performed recovering the rigid 2x2 cm^2 plates after 24 h time of reaction and washing them with butanol before the next run.

2.2.7. General procedure for the determination of the hydrogen yield from the dehydrogenative coupling of dimethylphenylsilane with alcohols

To measure H_2 evolution in silane-alcohol coupling, the experiments were conducted in a 130 ml reaction vessel under continuous stirring (250 rpm) at 25 °C. Control reactions of diphenylmethylsilane and *n*-butanol performed at 500 rpm give the same temporal profiles, indicating that the reaction is not under diffusion limitation. The vessel was sealed and the internal air is degassed thrice using argon. The catalysts (15 mg of Ru/G or 4 plates of $\overline{Ru}$(002–101)/G or $\overline{Ru}$(002)/G) were added to 8 ml of the alcohol in which 5 mmol of dimethylphenylsilane was dissolved immediately prior to the experiment. H_2 generation was followed by analyzing the gases on the headspace using an Agilent 490 MicroGC having two channels both of them with TC detector and using Ar as a carrier gas. One channel has a MolSieve 5A column and analyzes H_2. The second channel has a Pore Plot Q column and analyzes CO, CH4 and light hydrocarbons. Quantification of H_2 was based on prior calibration of the system using standard samples of known H_2 composition.

2.2.8. General procedure for the hydrogen transfer reduction of cyclohexanone

All reagents were purchased from Sigma-Aldrich and used as received without additional purification steps. To 1 mmol of cyclohexanone, 1.5 ml of the NaOH solution (2 mg of NaOH in 1.5 ml of isopropanol) is added followed by the addition of the catalyst (3 plates of $\overline{Ru}$(002–101)/G or $\overline{Ru}$(002)/G or 3 mg of Ru/G powder). The reaction was stirred at 250 rpm for 8 h at 80 °C. The catalyst was collected by filtration and the reaction products were analyzed using GC–MS using n-dodecane as internal standard.

3. Results and discussion

3.1. Catalysts preparation and characterization

The procedure herein used to prepare films containing Ru starts adsorbing $Ru(NH_3)_6Cl_3$ into alginate, the resulting viscous gel being cast on quartz plates (Scheme 1). These alginate films containing $Ru(NH_3)_6Cl_3$ were pyrolyzed in the absence of O_2. Photographs of the resulting films on quartz substrates are provided in Fig. S1 in supporting information.

After pyrolysis, the resulting Ru/G films were characterized by chemical analysis, X–ray diffraction (XRD), Raman, X-ray photoelectron spectroscopy (XPS) and microscopy techniques. For the sake of XRD characterization, we initially prepared films with a high percentage of Ru (20 %) to be able to record the diffractogram of Ru NPs. Fig. S2 of supporting information shows the scanning electron microscopy (SEM) images of the $\overline{Ru}$(002)/G that exhibits a smooth surface without cracks or pinholes in the underlying G film on top of which inhomogeneously distributed Ru NPs appear. Particle size distribution of Ru NPs reveals the presence of small (10 nm) and large (150 nm) particles with an average at 64.2 nm (Fig. S2 a, c inset). The XRD patterns of these samples (Fig. 1) shows that $\overline{Ru}$(002)/G film exhibits exclusively a narrow diffraction peak at 42° corresponding to the 002 facet of Ru metal, other diffraction peaks present in Ru metal are not present in $\overline{Ru}$(002)/G film. The absence of other diffraction peaks of Ru NPs is taken as a firm evidence of the preferential crystal growth. The broad diffraction peaks at 24 and 65° are characteristic of the G film.

When the synthesis to obtain Ru NPs supported on G films was carried out in an atmosphere containing 5 % H_2, the XRD pattern of the resulting $\overline{Ru}$(002–101)/G films exhibits, besides the 002 peak, the peak corresponding to the 101 facet. Worth noting is that other XRD peaks present in unoriented Ru NPs were also absent in

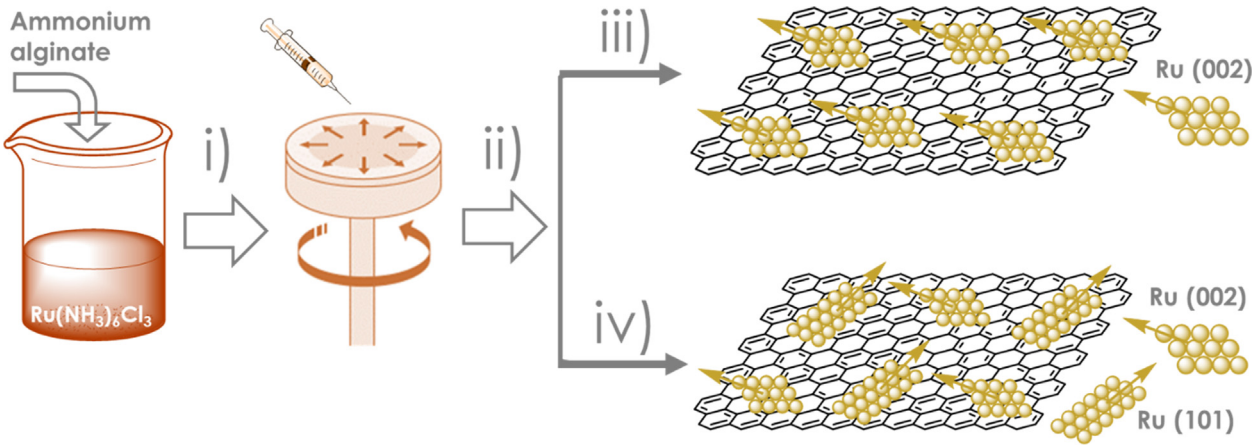

Scheme 1. Pictorial illustration of the preparation of $\overline{Ru}$(002)/G and $\overline{Ru}$(002–101)/G films. i) Formation of films of sodium alginate with adsorbed $Ru(NH_3)_6Cl_3$ by spin-coating; ii) Pyrolysis at 1000 °C; iii) in Ar atmosphere or iv) under 5% H_2/ 95% Ar atmosphere giving place to differently oriented Ru NPs over defective graphene films.

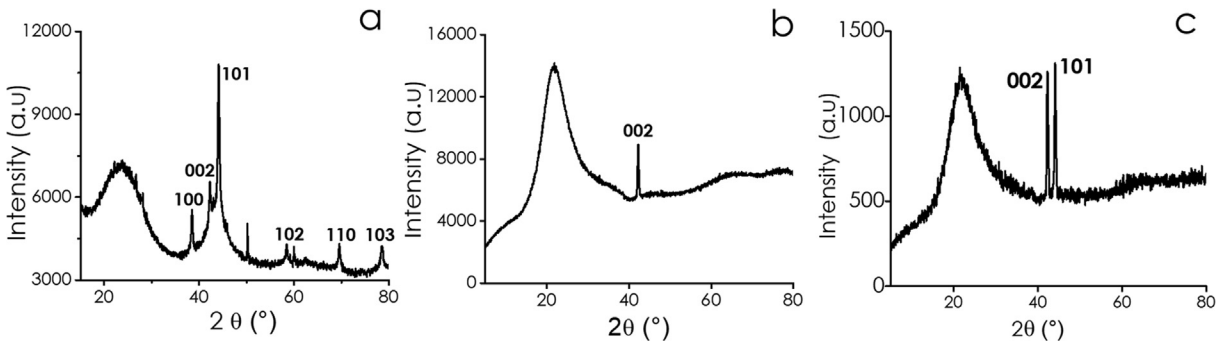

Fig. 1. XRD patterns of a) unoriented Ru NPs on G (5 wt% Ru) b) $\overline{Ru}$(002)/G and c) $\overline{Ru}$(002–101)/G. The broad peaks at 24° and 65° correspond to multilayer G.

$\overline{Ru}$(002–101)/G films. This indicates that molecular H_2 alters the crystal growth of Ru NPs. In addition, H_2 as reducing agent improves G quality, diminishing O content on G and improving the Raman spectra.[45] In contrast to the presence of one or two diffraction peaks for Ru NPs in $\overline{Ru}$(002)/G and $\overline{Ru}$(002–101)/G films, respectively, a control sample Ru/G (5 wt% Ru) obtained impregnating ammonium alginate beads with $RuCl_3$ solution and subsequent pyrolysis, exhibits the expected XRD of unoriented Ru NPs with all possible crystallographic planes. The influence of H_2 on Ru crystals observed here agrees with reports in the literature showing the reconstruction of Ru clusters in the presence of H_2 [46] and the change in the morphology of Ru particles in hydrogenation reactions frequently observed.[43] Although CO or even CO_2 evolving during the pyrolysis could also play a role on the crystal facet of Ru NPs in addition to graphene templating effect, comparison of the preparation in the absence and presence of H_2 shows the importance of this gas shaping the Ru crystal. In fact, the amount of H_2O, CO and CO_2 generated from a few micrograms of chitosan should be much minor in comparison with the steady 0.5 mmols of $H_2 \times min^{-1}$ constantly flushed into the pyrolysis reactor.

Having observed the orientation of the Ru NPs by XRD with samples with a high percentage of Ru, then we prepared samples with a lower percentage of Ru (5 % respect to ammonium alginate weight before pyrolysis) that will give rise to smaller NPs and a higher percentage of exposed Ru atoms on the surface, therefore being more active for catalysis. Scanning electron microscopy (SEM) images of the sample $\overline{Ru}$(002–101)/G (Fig. 2a,b) and $\overline{Ru}$(002)/G (Fig. 2c,d) at this low percentage, shows a smooth film surface in which Ru NPs are present with particle size distribution of Ru NPs with an average at 23 nm (Fig. 2 a, c inset). Note that if Ru atoms or clusters would be buried within the G film the surface would be expected to exhibit some roughness. For the sake of comparison, Fig. S.3 presents FESEM images and elemental EDX mapping of Ru/G control sample without preferential Ru NP orientation.

TEM images of $\overline{Ru}$(002)/G films reveal the presence of small Ru NPs from 1 to 10 nm not seen in FESEM (Fig. 3). EDX confirmed that the small NPs were Ru (Fig. S4-S5). Electron diffraction of Ru NPs shows that they are single crystals with an atomic distance of 2.12 Å, corresponding to Ru 002 plane (Fig. 3b), providing at microscopic level concordant information as XRD at macroscopic scale for larger Ru contents on the film. Worth noting is that the atomic distance corresponding to the Ru 002 plane was observed in TEM for all Ru NPs measured, regardless of their particle size (supporting information, Fig. S6-S7), meaning that the preferential crystallographic orientation was not specific of a certain particle size, but for all Ru NPs as implied in the XRD measurements for $\overline{Ru}$(002)/G of higher loading.

Analogous information as that of $\overline{Ru}$(002)/G was obtained for $\overline{Ru}$(002–101)/G films. However, two different atomic distances of 2.12 and 1.99 Å corresponding to the 002 and 101 planes, respectively, were measured in this case as well regardless of the particle size (Fig. 3d and Fig. S8, supporting information). TEM analysis of the control Ru/G film of unoriented Ru NPs shows, as the most remarkable difference respect to the Ru oriented films, the much smaller size of unoriented Ru NPs with 1 nm average (Fig. S9 in supporting information). The much smaller Ru NP size for Ru/G

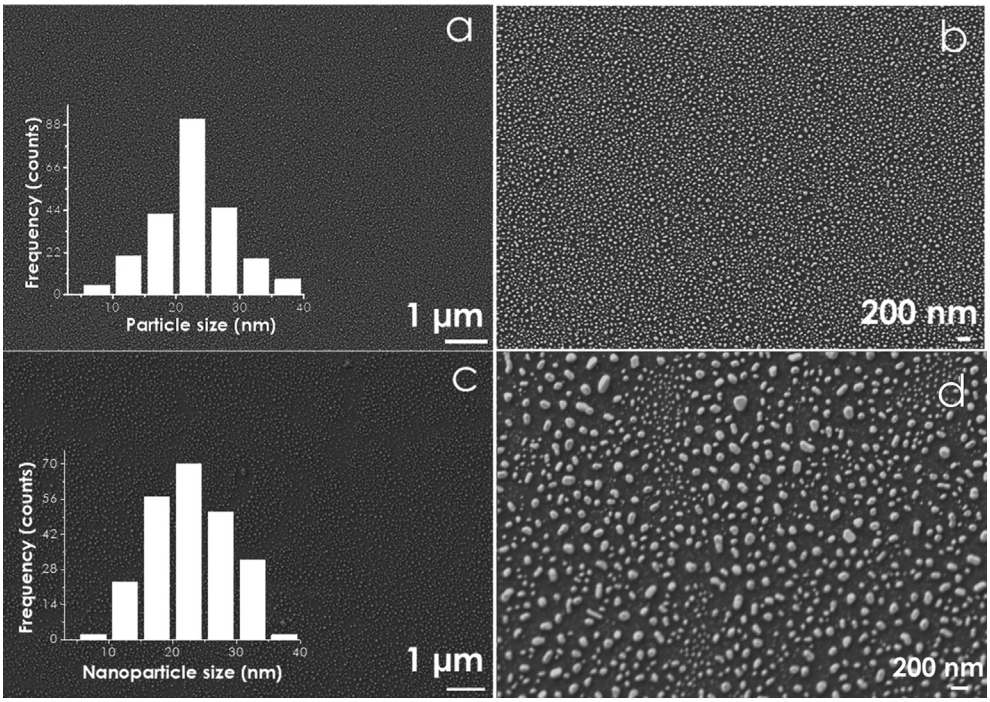

Fig. 2. SEM images of a), b) $\overline{Ru}$(002–101)/G and c), d) $\overline{Ru}$(002)/G at two magnifications. Insets: Size distribution histograms. The content of Ru vs. alginate in the preparation step was 5 %.

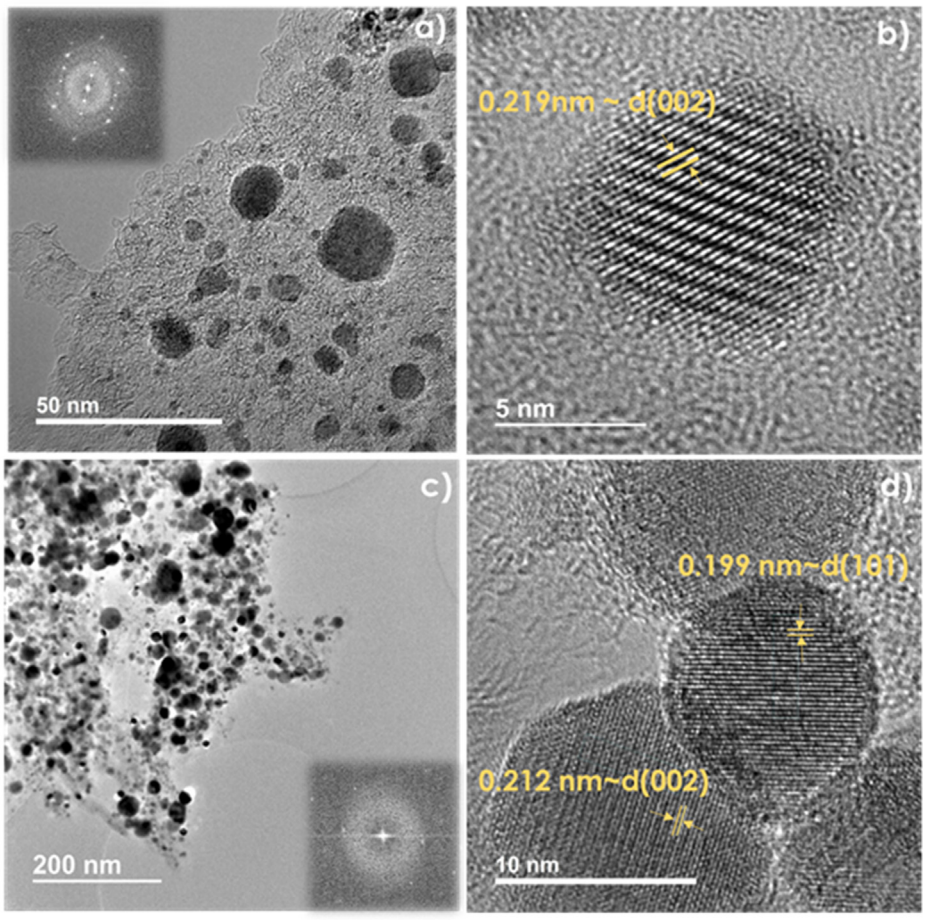

Fig. 3. a-b) TEM images of $\overline{Ru}$(002)/G at two magnifications. The atomic distance corresponds to the 002 facet; c-d) TEM images of $\overline{Ru}$(002–101)/G at two magnifications. Two atomic distances corresponding to the 002 and 101 facets of Ru were found. Insets show the corresponding selected area electron diffraction patterns.

powder could reflect the benefits of embedment of the nascent Ru NP within a carbon matrix wrapping the particles, rather than their support on a flat film surface. Considering the higher catalytic activity of small size NPs, it could be expected that control Ru/G sample should exhibit the highest activity compared to $\overline{Ru}$(002)/G and $\overline{Ru}$(002–101)/G (23 nm average size). Attempts to prepare oriented Ru NPs supported on defective graphene [either $\overline{Ru}$(002)/G or $\overline{Ru}$(002–101)/G depending on the presence of H_2] with smaller particle size and narrower particle size distribution were made by varying the pyrolysis temperature (900 and 1100 °C) and the percentage of H_2 in the flow (0, 5 and 10 %) during the pyrolysis. As expected the mean particle size increased with the temperature and was somewhat smaller under H_2, but the size distribution was still broad. Supporting information provides the TEM images and histograms of these screening tests (Figures S.10-S.18). As no evident advantage, samples prepared at 1000 °C in the absence or presence of 5 % H_2 were used in the evaluation of the catalytic activity.

Further details on the Ru NP morphology and film roughness and thicknesses were obtained by atomic force microscopy (AFM) with subnanometric vertical resolution (Fig. 4). According to AFM, the G layer for both $\overline{Ru}$(002)/G and $\overline{Ru}$(002–101)/G films at this resolution higher than SEM was smooth with a film thickness of about 15 nm. The presence of Ru NPs is clearly visualized in the frontal AFM views, with average Ru NP height of 4.3 and 7.6 nm for $\overline{Ru}$(002)/G and $\overline{Ru}$(002–101)/G, respectively (insets Fig. 4). The smoothness of the G films with subnanometric roughness suggests that Ru atoms or clusters are not buried within the G films. The difference in Ru NP height suggests that $\overline{Ru}$(002)/G and $\overline{Ru}$(002–101)/G films have in common the upper 002 facet, but differ on the height due to the 101 facet, less developed in $\overline{Ru}$(002)/G film than in $\overline{Ru}$(002–101)/G. Accordingly, H_2 makes Ru NPs grow in the height direction, developing the 101 facet.

XPS analyses of films of Ru deposited on G indicate the presence of C, O and Ru and the absence of Cl or Na. Cl or Na were also not detected by ICP. Coincidence of the $Ru3d_{3/2}$ and C1s peaks makes difficult a detailed analysis of C atoms on $\overline{Ru}$(002)/G (Fig. 5). Ru3d signal appears split into two peaks at binding energy 280.11 and 284.31 eV, attributable to $Ru3d_{5/2}$ and $Ru3d_{3/2}$, respectively. While the $Ru3d_{3/2}$ peak coincides with C1s, analysis of $Ru3d_{5/2}$ that does not overlap with any other element indicates a single component due to Ru(0). A shift in the binding energy of −0.19 eV respect to the standard $Ru3d_{5/2}$ value indicates that Ru (0) electronic density is higher than usual. This binding energy shift in XPS of oriented metal NPs on G has been taken in previous studies as a quantitative indicator of strong metal-support interaction through electron donation from G to the metal. In addition, XPS agrees with XRD that the film is constituted by metallic Ru NPs, ruthenium oxides being not detected.

Similar conclusions were drawn for $\overline{Ru}$(002–101)/G films. However, no binding energy shift in the Ru(0) peaks appearing at 280.30 and 284.53 eV respect to standard Ru(0) values was observed. In addition, a relative Ru surface atomic proportion about twice higher than that for $\overline{Ru}$(002)/G was measured. These features can be rationalized considering the higher Ru NP height in $\overline{Ru}$(002–101)/G, making interaction with the basal G plane weaker and surface Ru proportion higher than in $\overline{Ru}$(002)/G.

The defective nature of the graphene formed by alginate pyrolysis has been already reported in the literature and can be assessed by Raman spectroscopy (see Fig. 6). The Raman spectra show the presence of the 2D, G and D band characteristic of graphenes having defects in their basal planes [45]. These defects consist in the presence of oxygen functional groups and carbon vacancies [45]. Previous theoretical work with models have revealed the role of defects to establish strong metal-graphene interactions, as it may also be the case here [45].

3.2. Catalytic activity

Having shown the preparation of films containing Ru NPs with defined crystallographic planes, the study focused on the influence of the preferential orientation on the catalytic activity of Ru NPs. It is known that Ru can exhibit distinctive catalytic activity for hydrogenation reactions and ammonia synthesis depending on the facet exposed [47]. With this aim, two reactions, namely the dehydrogenative silane-alcohol coupling (Eq. 1) and the hydrogen transfer reduction of carbonyls (Eq. 2) were selected as model reactions to evaluate the relative activity of the film catalysts. The catalytic experiments were performed with $\overline{Ru}$(002)/G and $\overline{Ru}$(002–101)/G films with a loading of 1.34×10^{-9} and 1.76×10^{-9} $mol_{Ru} \times cm^{-2}$, respectively.

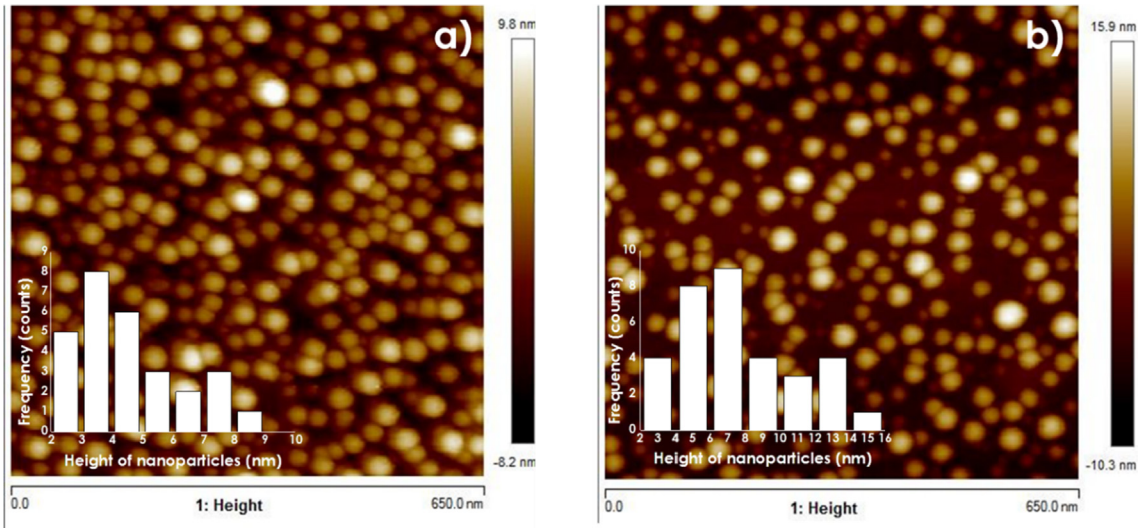

Fig. 4. AFM frontal views of a) $\overline{Ru}$(002)/G and b) $\overline{Ru}$(002–101)/G. Insets: Histograms of Ru NP height for both materials.

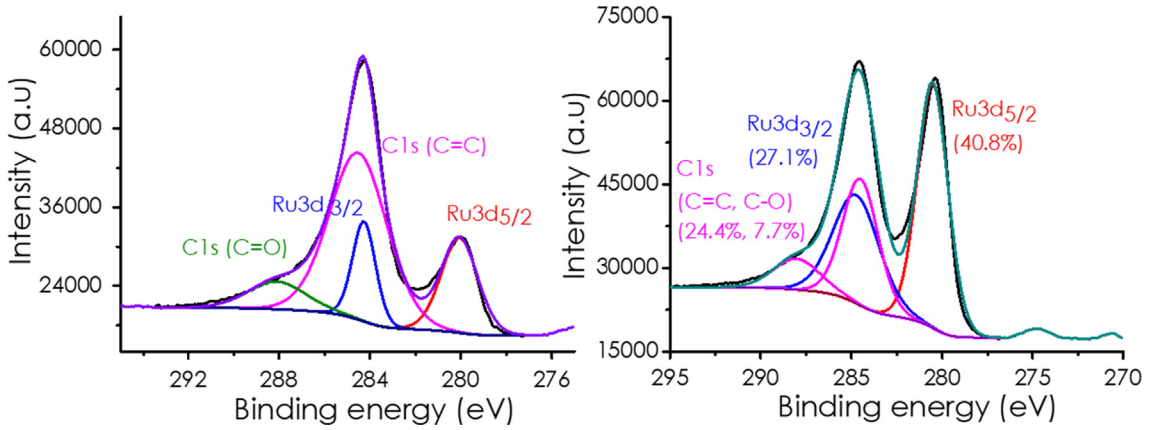

Fig. 5. High resolution XPS C1s and Ru3d peaks of $\overline{Ru}$(002)/G (a) and $\overline{Ru}$(002–101)/G (b) as well as the best deconvolution to individual components.

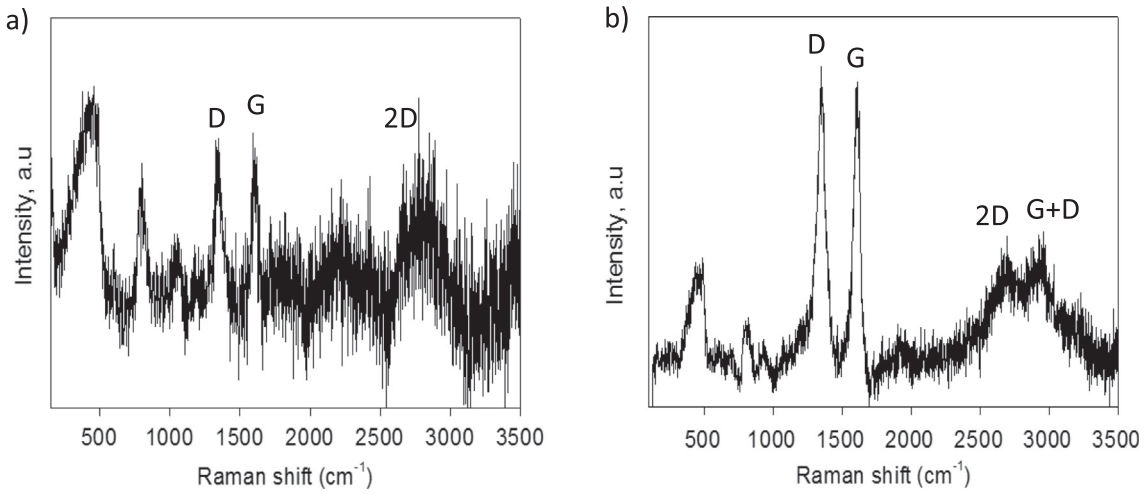

Fig. 6. Raman spectra of $\overline{Ru}$(002)/G (a) and $\overline{Ru}$(002–101)/G (b) films upon 514 nm excitation. The low signal to noise ratio of $\overline{Ru}$(002)/G probably reflects its lower thickness. The broad peaks at 470 nm is an artifact due to the quartz substrate.

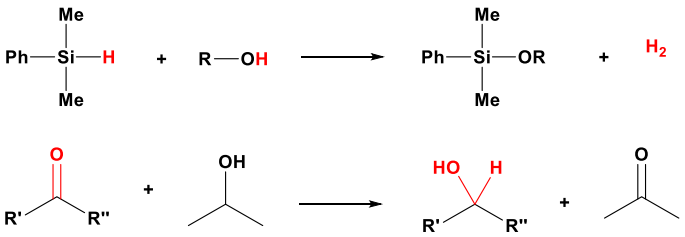

Coupling of silanes and alcohols to alkyl silyl ethers is of interest in view of the mild reaction conditions for *on-demand* H_2 generation from liquid carriers [48]. Initial tests were performed using control Ru/G powders in suspension as catalyst and dimethylphenylsilane reacting with different alcohols. To compare the activity of the three catalysts, turnover number (TON) and turnover frequencies (TOF) values were the figure of merit. Experimental section contains the equations used to determine TON and TOF values. TOFs were estimated at the same conversion level of 7 % for the three samples. High silane conversions and large TON and TOF values were achieved using Ru/G for aliphatic and benzylic alcohols (Table 1, entries 1 to 4). Evolution of H_2 in all cases was measured and quantified by analysis of the headspace gas. The values are also listed in Table 1. Formation of H_2 is in favor of the reported mechanism in which alcohol attacks nucleophilic to hydrosilane interacting with the Ru NP, resulting in the formation of Ru-H hydride and the protonated silyl ether, which undergoes a subsequent deprotonation [47].

Fig. S.19 in Supporting Information presents the time-conversion plots for the coupling of dimethylphenylsilane with different alcohols. Reusability tests for Ru/G show that the initial reaction rate and final conversion decrease gradually from 0.15 to 0.11 mmol $\times$ min^{-1} and from 98.9 to 76.2 %, respectively, in 5 uses. STEM analysis of the particle size after 5 runs indicates a growth from the initial 1 to 2 nm average size (Fig. S.20, Supporting Information), suggesting that partial deactivation of Ru/G is due to particle size increase under the reaction conditions.

Table 1
Reaction conditions and scope using Ru/G powders, $\overline{Ru}$(002–101)/G and $\overline{Ru}$(002)/G films as catalysts.

Entry	Catalyst	Alcohol	Conversion (%)	H_2 yield (%)[d]	TON	TOF (h^{-1})[e]
1[a]	Ru/G	Butanol	87	76	2928	815
2[a]	Ru/G	Pentanol	95	75	3194	798
3[a]	Ru/G	Hexanol	99	70	3329	832
4[a]	Ru/G	Benzyl alcohol	85	57	2877	719
5[b]	$\overline{Ru}$(002–101)/G	Butanol	25.4	8	48,068	12,017
6[b]	$\overline{Ru}$(002–101)/G	Pentanol	15.6	9	29,583	7395
7[b]	$\overline{Ru}$(002–101)/G	Hexanol	18.4	5	34,905	8726
8[b]	$\overline{Ru}$(002–101)/G	Benzyl alcohol	2.9	1	5587	1396
9[c]	$\overline{Ru}$(002)/G	Butanol	7.9	3	19,840	4960
10[c]	$\overline{Ru}$(002)/G	Pentanol	7.1	2	17,674	4418
11[c]	$\overline{Ru}$(002)/G	Hexanol	8.9	1	22,379	5594
12[c]	$\overline{Ru}$(002)/G	Benzyl alcohol	5.5	1	13,691	3422

[a] Reaction conditions: Me_2PhSiH (1 mmol), 1.5 ml of alcohol, 3 mg of Ru/G, 25 °C, 7 h. Conversion determined by GC analysis with n-$C_{12}H_{26}$ as internal standard; [b] Reaction conditions: same reagents and temperature as footnote "a", but using as catalyst three 1x1 cm^2 quartz plates coated with $\overline{Ru}$(002–101)/G (Ru content $1.76.10^{-9}$ mol × cm^{-2}, reaction time 24 h; [c] Reaction conditions: same reagents and temperature as footnote "a", but using as catalyst three 1 × 1 cm^2 quartz plates of $\overline{Ru}$(002)/G film (Ru content $1.34.10^{-9}$ mol × cm^{-2}), reaction time 24 h. [d] Reaction conditions: Me_2PhSiH (5 mmol), 7.5 ml of alcohol, catalysts: 15 mg of Ru/G, 4 plates of 2 × 2 cm^2 of $\overline{Ru}$(002–101)/G or $\overline{Ru}$(002)/G , 25 °C. [e] Determined at the same conversion of 7 %. The amount of H_2 was determined by micro GC analysis with prior calibration.

The reactions were also carried out using as catalyst 1x1 cm^2 quartz plates coated by nanometric thick films of G containing oriented Ru NPs. An additional control testing the activity of G films on quartz in the absence of Ru NPs under identical conditions showed no activity. In contrast, although phenyldimethylsilane conversions were lower, G films containing oriented Ru NPs exhibit a remarkable activity in terms of turnover number (TON) and turnover frequency (TOF), due to the minute Ru amount present in the films. $\overline{Ru}$(002)/G as catalyst afforded in 4 h at room temperature between 5.5 and 8.9 % silane conversion to its silyl ether (Table 1, entries 9–12). Considering the amount of Ru on the films of a few ng, TON values 6 to 9 times higher than those determined for Ru/G sample were measured. This increase in activity is even more remarkable considering that average Ru particle size in $\overline{Ru}$(002)/G is 23 nm, substantially larger than in fresh Ru/G (1 nm) and that the catalyst is not suspended, but deposited on a rigid quartz plate. Surface area and porosity are also in favor of Ru/G, since the oriented $\overline{Ru}$(002)/G are supported on a macroscopically flat film. Thus, although comparison between the activity of Ru/G and $\overline{Ru}$(002)/G should be taken cautiously due to the above commented differences, the positive catalytic features are all in favor of Ru/G that nevertheless has lower TON. The higher activity of $\overline{Ru}$(002)/G is clearly evidenced considering that the silane butanol coupling is being promoted by a few nanomols of Ru grafted on the defective graphene film. $\overline{Ru}$(002)/G films were notably stable and prolonging the experiment over 80 h resulted in conversions of about 80 % (see supporting information, Figures S.21-S.24).

A comparison of the intrinsic catalytic activity of different crystallographic facets in Ru NPs was obtained from the kinetic data of $\overline{Ru}$(002)/G and $\overline{Ru}$(002–101)/G. According to Table 1, conversion, TON and TOF values for the $\overline{Ru}$(002–101)/G film are significantly higher than for $\overline{Ru}$(002)/G. Fig. 7 presents the time-conversion plots for the reaction of Me_2PhSiH with butanol using Ru/G, $\overline{Ru}$(002–101)/G and $\overline{Ru}$(002)/G as catalysts, while Fig. S.25 in supporting information shows the time-conversion plots for the reaction of Me_2PhSiH with other alcohols. Note that although Ru/G apparently is more active in this Fig. 7, this is due to the higher Ru content, small average Ru particle size and large surface area of G. However, as indicated in Table 1, TON and TOF values of $\overline{Ru}$(002–101)/G and $\overline{Ru}$(002)/G are much higher. In principle, constant TON values, conversions and TOFs should be observed, unless one crystallographic facet is more active than the other one. Therefore, the significantly better performance of $\overline{Ru}$(002–101)/G indicates that the 101 facet is catalytically more active than the 002. Estimation based on the average particle size and height of Ru NPs indicates that the 101 facet is more than eight times more active than the 002 plane (supporting information).

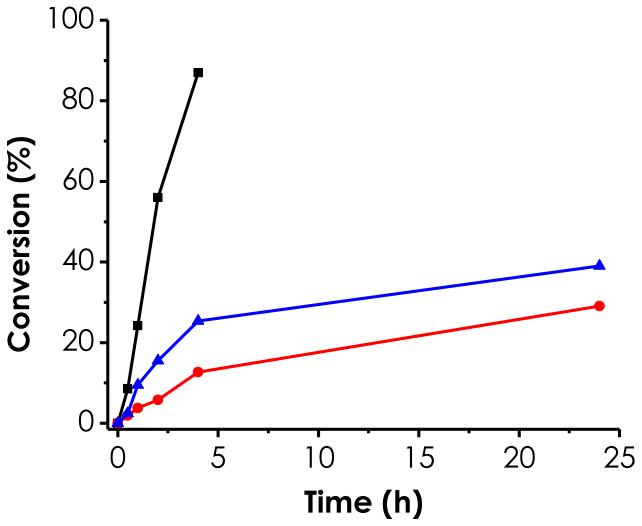

Fig. 7. Time-conversion plots for the dehydrogenative coupling of Me_2PhSiH with butanol catalysed by Ru/G (■), $\overline{Ru}$(002–101)/G (▲) and $\overline{Ru}$(002)/G (●). Reaction conditions: Me_2PhSiH (1 mmol), butanol (1.5 ml), 25 °C; Ru/G 3 mg, $\overline{Ru}$(002–101)/G and $\overline{Ru}$(002)/G three 1 × 1 cm^2 plates. For reaction conditions in each case,

A second use of both films of oriented Ru NPs on G shows some decrease in activity as determined by 24 h conversion (Fig. S.26, Supporting information). While the recycling experiments showed slight catalyst deactivation, we must stress the impressive long-term stability of $\overline{Ru}$(002–101)/G, as the latter remains active for 8 days allowing to reach a final TON value of 129,740 (see Fig. S.27 in supporting information).

To put the catalytic activity of $\overline{Ru}$(002–101)/G and $\overline{Ru}$(002)/G films into context, Table S1 provides a summary of the reported values compared to the results achieved in the present study. As it can be seen in this Table, $\overline{Ru}$(002–101)/G catalyst is the most active catalyst reported for this dehydrogenative silane-alcohol coupling.

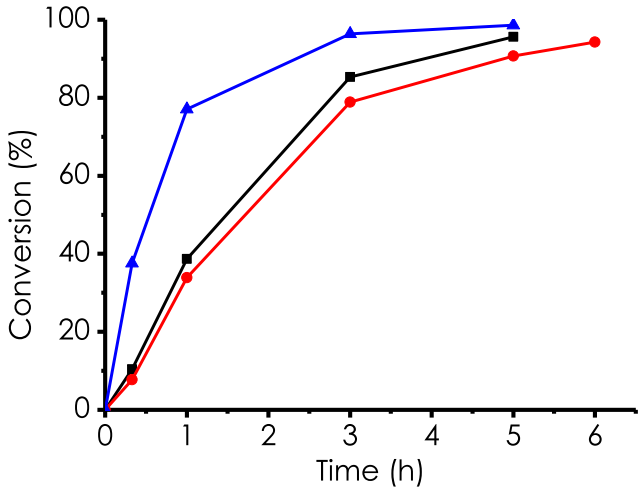

Fig. 8. Time-conversion plots for hydrogen transfer from isopropanol to cyclohexanone. Reaction conditions: cyclohexanone (1 mmol), isopropanol (1.5 ml), NaOH (1 mg), 80 °C. Catalyst: Ru/G as powder (3 mg) (●), $\overline{Ru}$(002)/G (■) and $\overline{Ru}$(002–101)/G (▲) (3 quartz 1 × 1 cm^2 plates), same Ru loading as Table 1.

The second reaction tested was the hydrogen transfer reduction of cyclohexanone to cyclohexanol in isopropanol as solvent and hydrogen donor [49,50]. For this reaction, the relative activity order of the samples was different, Ru/G being the less efficient catalyst (See Fig. 8). Taking initial reaction rates as the figure of merit of activity, values of 5.2, 18.7 and 3.8 μmol × min^{-1} $\overline{Ru}$(002)/G, $\overline{Ru}$(002–101)/G and Ru/G, respectively, were measured, corresponding to TOF values of 3880, 10,625 and 12.9 min^{-1} respectively, confirming the higher catalytic activity of oriented Ru NPs. It is proposed that the reaction occurs following the reported mechanism involving the Ru-H hydride formed from the Ru-alcoholate as the key reaction mechanism.

Estimations based on the average particle size and height of the Ru NPs indicate that the efficiency of the 101 facet is more than seven times that of the 002 plane.

Cyclohexanone reduction by isopropanol through H_2 transfer has been studied with numerous catalysts, including those containing Ru NPs. To put the catalytic activity of $\overline{Ru}$(002–101)/G and $\overline{Ru}$(002–101)/G films into context, Table S2 in supporting information summarizes the activity of some of the reported catalyst. As it can be seen in this Table S2, the TOF values achieved with $\overline{Ru}$(002–101)/G films are among the highest ever reported, ranking $\overline{Ru}$(002–101)/G films at the top of the most efficient catalysts for carbonyl reduction by hydrogen transfer from alcohols.

To put the activity of $\overline{Ru}$(002–101)/G films into context, Table S2 in the supporting information provides a comparison of the conversion, TON and TOF values measured for oriented films with those of benchmark catalysts reported in the literature. This comparison shows that $\overline{Ru}$(002–101)/G and $\overline{Ru}$(002)/G films are among the most active catalysts ever reported.

3.3. Theoretical calculations

Periodic DFT calculations were carried out to understand the preferential growth of Ru NPs as well as H_2 adsorption (see supporting information for details). First, clean Ru (002) and Ru (101) crystallographic planes (Fig. S.28, Supporting information) from hexagonal lattice were optimized without considering G. This optimization points towards a significant stability of (002) plane respect the (101) facet (ΔE = 1.46 eV). A theoretical relative rate between both planes of 4.7 (k_{002}/k_{101} ratio) was estimated. This would justify, why Ru NPs with a preferential (002) facet are observed under Ar atmosphere.

Adsorption phenomena strongly depends on adsorbate location on the surface [51]. To localize favorable adsorption sites, analyses of molecular electrostatic potential (MEP) surface were carried out. The calculated MEP surface reveals a significant difference between the (002) and the (101) planes (Fig. 9). The (002) plane exhibits positive regions (+1.1 and + 3.0 eV) on MEP surface, whereas (101) plane presents negative values (-1.3 and −2.4 eV). These MEP surfaces indicate a different behavior of Ru(002) and Ru(101) in the presence of H_2 or reagents for catalytic purposes.

Importantly, these positive and negative MEP surfaces are significantly attenuated by supporting Ru NPs on G. The interaction of Ru (002) on a G layer shows short distances (2.19 – 2.26 Å), indicating a strong interaction energy of −2.35 eV [-1.75 eV for Ru (101)]. Since this (002)-facet is the most stable and interacts stronger with G, its growth is expected under Ar (E_{ads} = 0.67 eV). In addition, the fact that for the (002) facet the MEP is close to zero in comparison to the (101) model that shows positive and negative regions suggest that, in principle, this plane should be more favorable for interaction with H_2.

However, a different situation arises in the presence of H_2. Both, Ru (002) and Ru (101) planes promote dissociative adsorption [$d_{H\cdots H}$ = 1.68 and 1.42 Å for (002) and (101), respectively]. Energetically, this process is more favorable for Ru (101) than Ru (002) from −0.49 to −0.28 eV, an order that follows the trend of the catalytic activity, Ru(101) facet being more active than Ru (002). Moreover, H_2 dissociation is responsible for inhibiting the growth of the first-appearing Ru(002) facet, favoring development of the Ru(101) plane, by restructuration of Ru(002) plane to the Ru(101) facet as consequence of the larger H_2 adsorption energy. Structural changes on Ru cluster upon H_2 adsorption have been rationalized similarly [46]. Therefore, the previous calculations provide a way to rationalize the differences in the crystallinity of Ru NPs supported on defective graphene depending on the pyrolysis atmosphere. Thus, under inert atmosphere the 002 facet develops, because it is the thermodynamically more stable Ru facet. In contrast, in the presence of H_2, the stronger dissociation energy of this gas on the 101 facet respect to the 002 planes would determine its growth.

The difference in H_2 adsorption for the Ru 002 and 101 facets as a scaling relationship can also serve to rationalize the higher catalytic activity of the $\overline{Ru}$(002–101)/G vs. $\overline{Ru}$(002)/G. According to the Sabatier principle, it is proposed that the stronger the H_2 adsorption on one specific facet, the stronger would be the catalytic activity that requires substrate adsorption. In this way, calculated H_2 adsorption strength could be used as a simple indicator of the catalytic activity. It should be reminded that H_2 is a reaction product in the case of silane-alcohol coupling and Ru-H are involved in the H transfer from isopropanol to cyclohexanone.

Nanometric thin films on flat quartz supports are not suitable for conventional H_2 adsorption measurements. For this reason, Raman spectra were recorded to provide some experimental support to the stronger interaction with H_2 of the 101 facet of Ru respect to the 002 plane. Raman spectra of $\overline{Ru}$(002–101)/G and $\overline{Ru}$(002)/G films were recorded under Ar and under H_2 atmosphere. The four Raman spectra are presented in Fig. S29 of the supporting information. While no changes were observed in the Raman spectra recorded under Ar or H_2 for $\overline{Ru}$(002)/G film, in the case of $\overline{Ru}$(002–101)/G appearance of two new vibration bands under H_2 not observed under Ar was recorded. These two new bands are attributed to vibration of Ru-H bonds on the 101 facet and, they were detected only for $\overline{Ru}$(002–101)/G film and not for $\overline{Ru}$(002)/G. The vibration position of these two bands at about

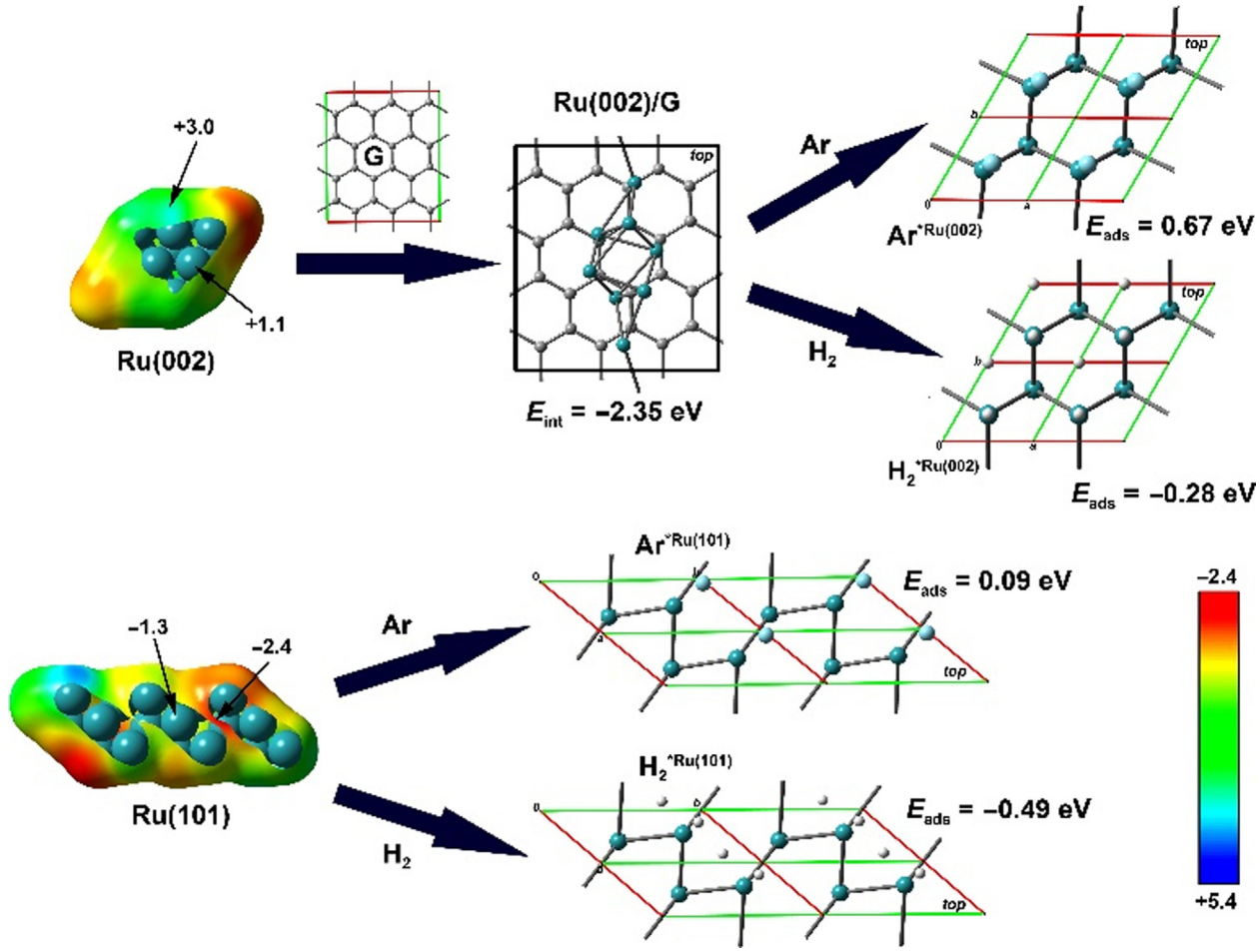

Fig. 9. MEP surface plotted on the van der Waals surface (0.001 a.u.) for Ru(002) and Ru(101) planes. Optimized structures of adsorbed gases (H_2 and Ar) on (002) and (101) planes are also displayed (H_2/Ar*Ru(002) and H_2/Ar*Ru(101), respectively). The scale bar and the values of potential (Vmax) and energies are given in eV.

1110 and 1020 cm^{-1} is compatible with previous reports for Ru-H species on carbon appearing at 1230 and 1070 cm^{-1} [52].

4. Conclusions

Nanometer-thick films of defective G containing Ru NPs with 002 or 002 and 101 facets can be obtained depending on the presence or not of H_2 in the pyrolysis. Calculations indicate that higher adsorption energy favors 101 facet growth. These oriented Ru NPs strongly grafted on G exhibit an enhanced catalytic activity for the dehydrogenative silane-alcohol coupling and hydrogen transfer reduction of cyclohexanone, compared to small Ru NPs (1 nm) without preferential orientation. Estimation of the intrinsic catalytic activity of the 002 and 101 planes shows that the latter one is five to eight times more active than the former one, TON and TOF values for $\overline{Ru}$(002–101)/G being higher than those of $\overline{Ru}$(002)/G. Overall, the present study illustrates a methodology to obtain metal NPs with preferential plane orientations strongly bound to G.

Declaration of Competing Interest

The authors declare that they have no known competing financial interests or personal relationships that could have appeared to influence the work reported in this paper.

Acknowledgements

Support by the Ministerio de Ciencia e Innovación (Severo Ochoa and RTI2018-098237-B-C21) and Generalitat Valenciana (Prometeo 2017/083) is acknowledged. Thanks are due to Galicia Supercomputing Center. AA thanks UEMF and UPV for an Erasmus + 2019-1-ES01-KA107-062073 Scholarship.

Appendix A. Supplementary material

Supplementary data to this article can be found online at https://doi.org/10.1016/j.jcat.2022.02.007.

References

[1] D. Astruc, Nanoparticles and catalysis, John Wiley & Sons, 2008.
[2] A. Cao, R. Lu, G. Veser, Stabilizing metal nanoparticles for heterogeneous catalysis, Phys. Chem. Chem. Phys. 12 (41) (2010) 13499, https://doi.org/10.1039/c0cp00729c.
[3] N. Dimitratos, J.A. Lopez-Sanchez, G.J. Hutchings, Selective liquid phase oxidation with supported metal nanoparticles, Chem. Sci. 3 (1) (2012) 20–44.
[4] K. An, G.A. Somorjai, Size and shape control of metal nanoparticles for reaction selectivity in catalysis, ChemCatChem 4 (10) (2012) 1512–1524.
[5] M. Moreno-Mañas, R. Pleixats, Formation of Carbon−Carbon Bonds under Catalysis by Transition-Metal Nanoparticles, Acc. Chem. Res. 36 (8) (2003) 638–643.
[6] J. Ohyama, R. Kanao, A. Esaki, A. Satsuma, Conversion of 5-hydroxymethylfurfural to a cyclopentanone derivative by ring rearrangement over supported Au nanoparticles, Chem. Commun. 50 (42) (2014) 5633–5636.
[7] Y.-S. Shon, H. Choo, Organic reactions of monolayer-protected metal nanoparticles, C. R. Chim. 6 (8-10) (2003) 1009–1018.

[8] B.R. Cuenya, Synthesis and catalytic properties of metal nanoparticles: Size, shape, support, composition, and oxidation state effects, Thin Solid Films 518 (12) (2010) 3127–3150.
[9] S. Zhang, X.u. Zhang, G. Jiang, H. Zhu, S. Guo, D. Su, G. Lu, S. Sun, Tuning Nanoparticle Structure and Surface Strain for Catalysis Optimization, J. Am. Chem. Soc. 136 (21) (2014) 7734–7739.
[10] Q.-L. Zhu, J. Li, Q. Xu, Immobilizing Metal Nanoparticles to Metal-Organic Frameworks with Size and Location Control for Optimizing Catalytic Performance, J. Am. Chem. Soc. 135 (28) (2013) 10210–10213.
[11] M. Haruta, Catalysis of gold nanoparticles deposited on metal oxides, Cattech 6 (2002) 102–115.
[12] T. Ishida, N. Kinoshita, H. Okatsu, T. Akita, T. Takei, M. Haruta, Influence of the Support and the Size of Gold Clusters on Catalytic Activity for Glucose Oxidation, Angew. Chem. Int. Ed. 47 (48) (2008) 9265–9268.
[13] G. Schmid, Large clusters and colloids. Metals in the embryonic state, Chem. Rev. 92 (8) (1992) 1709–1727.
[14] K. Zhou, Y. Li, Catalysis Based on Nanocrystals with Well-Defined Facets, Angew. Chem. Int. Ed. 51 (3) (2012) 602–613.
[15] A.R. Tao, S. Habas, P. Yang, Shape Control of Colloidal Metal Nanocrystals, Small 4 (3) (2008) 310–325.
[16] E. Ramirez, L. Eradès, K. Philippot, P. Lecante, B. Chaudret, Shape Control of Platinum Nanoparticles, Adv. Funct. Mater. 17 (13) (2007) 2219–2228.
[17] Y. Xia, Y. Xiong, B. Lim, S. Skrabalak, Shape-Controlled Synthesis of Metal Nanocrystals: Simple Chemistry Meets Complex Physics?, Angew Chem. Int. Ed. 48 (1) (2009) 60–103.
[18] Y. Xiong, Y. Xia, Shape-Controlled Synthesis of Metal Nanostructures: The Case of Palladium, Adv. Mater. 19 (20) (2007) 3385–3391.
[19] B. Wu, N. Zheng, G. Fu, Small molecules control the formation of Pt nanocrystals: a key role of carbon monoxide in the synthesis of Pt nanocubes, Chem. Commun. 47 (3) (2011) 1039–1041.
[20] X. Huang, S. Tang, X. Mu, Y. Dai, G. Chen, Z. Zhou, F. Ruan, Z. Yang, N. Zheng, Freestanding palladium nanosheets with plasmonic and catalytic properties, Nat. Nanotechnol. 6 (1) (2011) 28–32.
[21] J. Ren, R.D. Tilley, Preparation, Self-Assembly, and Mechanistic Study of Highly Monodispersed Nanocubes, J. Am. Chem. Soc. 129 (11) (2007) 3287–3291.
[22] J. Ren, R. Tilley, Shape-Controlled Growth of Platinum Nanoparticles, Small 3 (9) (2007) 1508–1512.
[23] L.M. Falicov, G.A. Somorjai, Correlation between catalytic activity and bonding and coordination number of atoms and molecules on transition metal surfaces: Theory and experimental evidence, Proc. Natl. Acad. Sci. U. S. A. 82 (8) (1985) 2207–2211.
[24] S. Liu, H. Tao, L.i. Zeng, Q.i. Liu, Z. Xu, Q. Liu, J.-L. Luo, Shape-Dependent Electrocatalytic Reduction of CO2 to CO on Triangular Silver Nanoplates, J. Am. Chem. Soc. 139 (6) (2017) 2160–2163.
[25] D. Mateo, J. Albero, H. García, Photoassisted methanation using Cu2O nanoparticles supported on graphene as a photocatalyst, Energy Environ. Sci. 10 (11) (2017) 2392–2400.
[26] N. Zhang, M.-Q. Yang, S. Liu, Y. Sun, Y.-J. Xu, Waltzing with the Versatile Platform of Graphene to Synthesize Composite Photocatalysts, Chem. Rev. 115 (18) (2015) 10307–10377.
[27] C. Han, N. Zhang, Y.-J. Xu, Structural diversity of graphene materials and their multifarious roles in heterogeneous photocatalysis, Nano Today 11 (3) (2016) 351–372.
[28] M.-Q. Yang, N. Zhang, M. Pagliaro, Y.-J. Xu, Artificial photosynthesis over graphene–semiconductor composites. Are we getting better?, Chem Soc. Rev. 43 (24) (2014) 8240–8254.
[29] A. Dhakshinamoorthy, I. Esteve Adell, A. Primo, H. Garcia, Enhanced Activity of Ag Nanoplatelets on Few Layers of Graphene Film with Preferential Orientation for Dehydrogenative Silane-Alcohol Coupling, ACS Sustain, Chem. Eng. 5 (3) (2017) 2400–2406.
[30] D. Mateo, I. Esteve-Adell, J. Albero, A. Primo, H. García, Oriented 2.0.0 Cu2O nanoplatelets supported on few-layers graphene as efficient visible light photocatalyst for overall water splitting, Appl. Catal. B Environ 201 (2017) 582–590.
[31] N. Candu, A. Dhakshinamoorthy, N. Apostol, C. Teodorescu, A. Corma, H. Garcia, V.I. Parvulescu, Oriented Au nanoplatelets on graphene promote Suzuki-Miyaura coupling with higher efficiency and different reactivity pattern than supported palladium, J. Catal. 352 (2017) 59–66.
[32] D. Mateo, I. Esteve-Adell, J. Albero, J.F.S. Royo, A. Primo, H. Garcia, 111 oriented gold nanoplatelets on multilayer graphene as visible light photocatalyst for overall water splitting, Nat. Commun 7 (2016) 11819.
[33] A. Primo, I. Esteve-Adell, S.N. Coman, N. Candu, V.I. Parvulescu, H. Garcia, One-Step Pyrolysis Preparation of 1.1.1 Oriented Gold Nanoplatelets Supported on Graphene and Six Orders of Magnitude Enhancement of the Resulting Catalytic Activity, Angew. Chem. Int. Ed. 55 (2016) 607–612.
[34] A. Primo, I. Esteve-Adell, J.F. Blandez, A. Dhakshinamoorthy, M. Álvaro, N. Candu, S.M. Coman, V.I. Parvulescu, H. García, High catalytic activity of oriented 2.0.0 copper(I) oxide grown on graphene film, Nat. Commun 6 (2015) 8561.
[35] I. Esteve-Adell, N. Bakker, A. Primo, E. Hensen, H. García, Oriented Pt Nanoparticles Supported on Few-Layers Graphene as Highly Active Catalyst for Aqueous-Phase Reforming of Ethylene Glycol, ACS Appl. Mater. Interfaces 8 (49) (2016) 33690–33696.
[36] Q. Zhang, H. Wang, Facet-Dependent Catalytic Activities of Au Nanoparticles Enclosed by High-Index Facets, ACS Catal. 4 (11) (2014) 4027–4033.
[37] Q. Zhang, Y. Zhou, E. Villarreal, Y.e. Lin, S. Zou, H. Wang, Faceted Gold Nanorods: Nanocuboids, Convex Nanocuboids, and Concave Nanocuboids, Nano Lett. 15 (6) (2015) 4161–4169.
[38] N.a. Tian, Z.-Y. Zhou, S.-G. Sun, Platinum Metal Catalysts of High-Index Surfaces: From Single-Crystal Planes to Electrochemically Shape-Controlled Nanoparticles, J. Phys. Chem. C 112 (50) (2008) 19801–19817.
[39] L. Hu, Q. Peng, Y. Li, Selective Synthesis of Co3O4 Nanocrystal with Different Shape and Crystal Plane Effect on Catalytic Property for Methane Combustion, J. Am. Chem. Soc. 130 (48) (2008) 16136–16137.
[40] X. Peng, S.G. Karakalos, W.E. Mustain, Preferentially Oriented Ag Nanocrystals with Extremely High Activity and Faradaic Efficiency for CO2 Electrochemical Reduction to CO, ACS Appl. Mater. Interfaces 10 (2) (2018) 1734–1742.
[41] H. Sun, H.M. Ang, M.O. Tadé, S. Wang, Co3O4 nanocrystals with predominantly exposed facets: synthesis, environmental and energy applications, J. Mater. Chem. A 1 (46) (2013) 14427.
[42] C.-Y. Chiu, P.-J. Chung, K.-U. Lao, C.-W. Liao, M.H. Huang, Facet-Dependent Catalytic Activity of Gold Nanocubes, Octahedra, and Rhombic Dodecahedra toward 4-Nitroaniline Reduction, J. Phys. Chem. C 116 (44) (2012) 23757–23763.
[43] L. Liu, M. Yu, B.o. Hou, Q. Wang, B. Zhu, L. Jia, D. Li, Morphology evolution of fcc Ru nanoparticles under hydrogen atmosphere, Nanoscale 11 (16) (2019) 8037–8046.
[44] S. Frindy, A. El Kadib, M. Lahcini, A. Primo, H. García, Isotropic and Oriented Copper Nanoparticles Supported on Graphene as Aniline Guanylation Catalysts, ACS Catal. 6 (6) (2016) 3863–3869.
[45] J. He, A. Anouar, A. Primo, H. García, Quality Improvement of Few-Layers Defective Graphene from Biomass and Application for H2 Generation, Nanomaterials 9 (6) (2019) 895.
[46] D. Bumüller, A.-S. Hehn, E. Waldt, R. Ahlrichs, M.M. Kappes, D. Schooss, Ruthenium Cluster Structure Change Induced by Hydrogen Adsorption: Ru19–, J. Phys. Chem. C 121 (20) (2017) 10645–10652.
[47] M. Zhao, A.O. Elnabawy, M. Vara, L. Xu, Z.D. Hood, X. Yang, K.D. Gilroy, L. Figueroa-Cosme, M. Chi, M. Mavrikakis, Y. Xia, Facile Synthesis of Ru-Based Octahedral Nanocages with Ultrathin Walls in a Face-Centered Cubic Structure, Chem. Mater. 29 (2017) 9227–9237.
[48] D. Ventura-Espinosa, A. Carretero-Cerdán, M. Baya, H. García, J.A. Mata, Catalytic Dehydrogenative Coupling of Hydrosilanes with Alcohols for the Production of Hydrogen On-demand: Application of a Silane/Alcohol Pair as a Liquid Organic Hydrogen Carrier, Chem. Eur. J. 23 (2017) 10815–10821.
[49] J. Long, Y. Zhou, Y. Li, Transfer hydrogenation of unsaturated bonds in the absence of base additives catalyzed by a cobalt-based heterogeneous catalyst, Chem. Commun. 51 (2015) 2331–2334.
[50] J. Long, K. Shen, L. Chen, Y. Li, Multimetal-MOF-derived transition metal alloy NPs embedded in an N-doped carbon matrix: highly active catalysts for hydrogenation reactions, J. Mater. Chem. A 4 (2016) 10254–10262.
[51] R. Berthoud, P. Délichère, D. Gajan, W. Lukens, K. Pelzer, J.-M. Basset, J.-P. Candy, C. Copéret, Hydrogen and oxygen adsorption stoichiometries on silica supported ruthenium nanoparticles, J. Catal. 260 (2008) 387–391.
[52] J.L. Blackburn, C. Engtrakul, J.B. Bult, K. Hurst, Y. Zhao, Q. Xu, P.A. Parilla, L.J. Simpson, J.-D.-R. Rocha, M.R. Hudson, C.M. Brown, T. Gennett, Spectroscopic Identification of Hydrogen Spillover Species in Ruthenium-Modified High Surface Area Carbons by Diffuse Reflectance Infrared Fourier Transform Spectroscopy, The Journal of Physical Chemistry C 116 (2012) 26744–26755.